2012

Growth mechanism and magnetic properties of highly crystalline NiO nanocubes and nanorods fabricated by evaporation

Dapeng Chen
University of Wollongong, dapeng@uow.edu.au

Xiaolin Wang
University of Wollongong, xiaolin@uow.edu.au

Yi Du
University of Wollongong, ydu@uow.edu.au

Song Ni
The University of Sydney, New South Wales, Australia

Zi-Bin Chen
The University of Sydney, New South Wales, Australia

See next page for additional authors

Publication Details

Chen, D., Wang, X., Du, Y., Ni, S., Chen, Z. & Liao, X. (2012). Growth mechanism and magnetic properties of highly crystalline NiO nanocubes and nanorods fabricated by evaporation. Crystal Growth and Design, 12 (6), 2842-2849.

CRYSTAL GROWTH & DESIGN

Article

pubs.acs.org/crystal

Growth Mechanism and Magnetic Properties of Highly Crystalline NiO Nanocubes and Nanorods Fabricated by Evaporation

Da-Peng Chen,[†] Xiao-Lin Wang,*[,†] Yi Du,[†] Song Ni,[‡] Zi-Bin Chen,[‡] and Xiaozhou Liao[‡]

[†]Institute for Superconducting and Electronic Materials, Innovation Campus, University of Wollongong, New South Wales 2519, Australia

[‡]School of Aerospace, Mechanical & Mechatronic Engineering, The University of Sydney, New South Wales 2006, Australia

Supporting Information

ABSTRACT: A new approach to the preparation of regularly shaped NiO nanocubes and nanorods by an infrared heating evaporation method is presented. The growth model is proposed to be a vapor−solid mechanism. The morphology of the nanocrystals can be tuned by the carrier gas flow rate. The samples consist of nanocrystals that are highly crystallized with atomic-scale smooth surfaces. This novel method could be extended to nanocrystal growth of other oxides with low volatility or high melting points. The results of magnetic characterization indicate that the NiO nanorods and nanocubes grown from a mixed target both show weak ferromagnetic states at low and room temperature due to uncompensated spins at the surfaces of the nanocrystals.

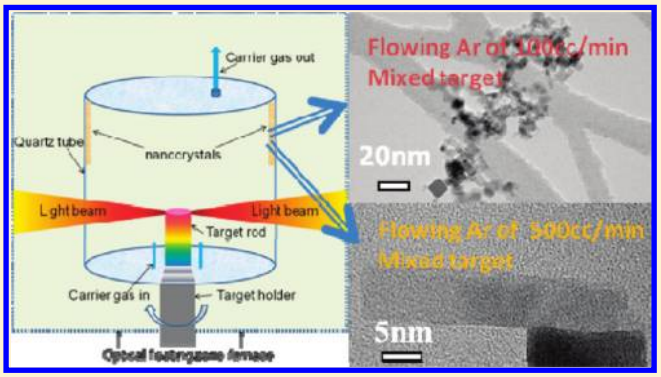

INTRODUCTION

Transition-metal oxides have been extensively investigated due to their significant importance in both fundamental research and applications.[1−3] Among the various oxides, NiO has been particularly studied as a promising candidate for the next generation of resistive switching memory devices.[4−6] The simple structure and high Néel temperature (T_N = 523 K) of NiO also make it a promising exchange-bias material. Ultrafast optical manipulation of spin and the dynamics in this material have been carefully studied in recent years.[7,8] Nickel oxide crystallizes in the face-centered cubic structure. The bulk magnetic structure of pure NiO is well accepted with the ferromagnetic sheets of Ni^{2+} aligned parallel to the (111) planes and antiferromagnetically aligned with respect to each other, while the magnetic moments of Ni^{2+} within each plane lie in the $\langle 11\bar{2} \rangle$ direction.[9−12] The fabrication and understanding of the properties of nanosize NiO play a key role in materials science, physics, and other research areas. Nanosized NiO can be used in rechargeable battery cathodes,[13,14] electrochemical capacitors,[15,16] catalysis,[17] gas sensors,[18] biomedical applications,[19] and magnetic materials. The properties of such nanomaterials are related to their chemical stoichiometry, defect distribution, size, and morphology, which strongly depend on the preparation conditions.[20,21] Compared with the amorphous or less crystallized nanomaterials, highly crystallized nanomaterials provide powerful research tools for deeper understanding of interesting properties in this material. Many methods have been developed to synthesize NiO nanomaterials with different shapes and morphologies,[15,22−28] but most experiments only yield relatively large particles (>20 nm) with relatively low crystallinity.

Early research has revealed that NiO is not directly suitable for evaporation techniques,[29] but in this paper, we report for the first time an infrared heating evaporation method to prepare NiO nanocrystals directly from a pure NiO target and from a NiO−TiO_2 mixed target by using an optical floating zone furnace under different atmospheres. Cubic-shaped NiO nanoparticles with an average width of 8 nm and tetragonal nanorods with a width of 6 nm and aspect ratio of 2−6 can be obtained by controlling the carrier gas flow rate from the mixed target. This method shows great potential for the synthesis of highly crystalline nanomaterials, especially for the materials with lower vapor pressure and high melting point. The magnetic properties of these NiO nanocrystals are also reported.

EXPERIMENTAL SECTION

The growth of nanocrystals was performed in a Crystal System Inc. infrared radiation furnace equipped with four 300 W tungsten halogen lamps (JIH 100V-300WC-CS). The heating area temperature and the temperature distribution along the inner wall of the quartz tube were calibrated by a thermocouple located in an alumina tube before the experiments so that the growth temperature could be determined.

In order to protect the target from being broken during growth, pure NiO (99.8%) powder was pressed into a 6 mm diameter rod and sintered overnight at 1150 °C, and a 30 mm long solid rod was then

Received: December 19, 2011
Revised: April 11, 2012
Published: April 17, 2012

cut to serve as the target. The mixed target was prepared by the conventional solid-state method. Powders of TiO_2 (99.8%) and NiO (99.8%) were mixed in the molar ratio Ti/Ni = 1.00:1.05. The mixture was calcined at 1150 °C for 6 h in air atmosphere and finally cooled to room temperature. The obtained polycrystalline powder was reground and formed into cylindrical rods 8 mm in diameter and 80 mm in length. The rods were hydrostatically pressed under a pressure of ~70 MPa and then sintered at 1350 °C for 20 h in air. After sintering, a rod 20 mm in length was cut to serve as the target. A schematic illustration of the growth apparatus is shown in Figure 1.

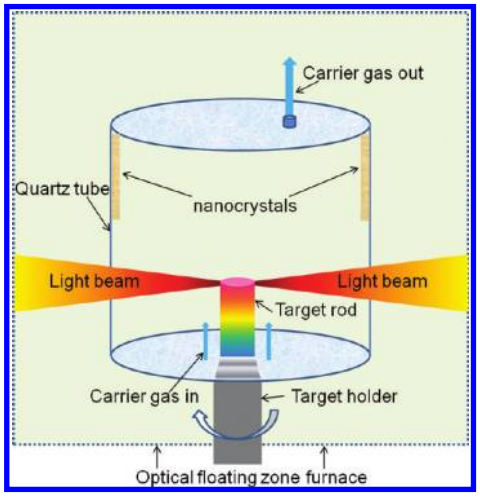

Figure 1. Schematic illustration of apparatus used in experiment.

The target rod was mounted on the sample holder and then sealed in a quartz tube with an inner diameter of 46 mm. Prior to heating the target, the top of the target was adjusted to the lower level of the heating area. Then, the temperature of the heating area was rapidly increased to the set point within 6 min. The target rod was moved upward through the heating area with a speed of 1 mm/h after the temperature reached the set point, accompanied by rotation of the target rod at 20 rpm. The growth time was typically 6–24 h. When evaporated directly from the pure NiO target, nanocrystals were grown in vertically flowing oxygen and argon with a 100 cc/min flow rate from the bottom to the top. When evaporated from the mixed target, nanocrystals were prepared in vertically flowing oxygen (100 cc/min) and argon (100 and 500 cc/min) from the bottom to the top. The NiO was evaporated from the targets, and the nanocrystals were deposited on the inner wall of the quartz tube above the heating area. The gray-green products could then be easily collected.

The phase purity of the NiO nanocrystals was examined by using powder X-ray diffraction (XRD). The morphology and composition were characterized by field emission scanning electron microscopy (FE-SEM) and energy-dispersive X-ray (EDX) spectroscopy (JEOL 7500). Transmission electron microscopy (TEM) and selected area electron diffraction (SAED) characterization of the samples were carried out on a JEM-3000F instrument operated at 300 kV. The samples were prepared by spreading an ultrasonicated suspension in ethanol onto a Cu grid coated with a holey carbon film. The magnetic properties were measured with a vibrating sample magnetometer (VSM) in a Physical Properties Measurement System (PPMS, Quantum Design) in the temperature range of 5–305 K. The samples (12–67 mg) were sealed in plastic wrap and then mounted on a sample holder.

■ RESULTS AND DISCUSSION

The growth of nanocrystals directly from the pure NiO target was performed at approximately 1600 °C under a carrier gas flow rate of 100 cc/min. The products were formed on the inner wall of the quartz tube, downstream of the carrier gas at a distance of 10–180 mm from the middle of the heating area, where the growth temperature was estimated to be in the range of 150–500 °C. After 6 h of growth, more than 70 and 45 mg of product were obtained under flowing oxygen and argon, respectively. The EDX patterns (Figure S1, Supporting Information) of the nanocrystals show only peaks of C, O, and Ni, confirming the formation of pure NiO, because such C peaks originate from the conductive carbon tape.

The influence of the atmosphere on the growth of the nanocrystals was investigated. Figure 2 shows the XRD patterns

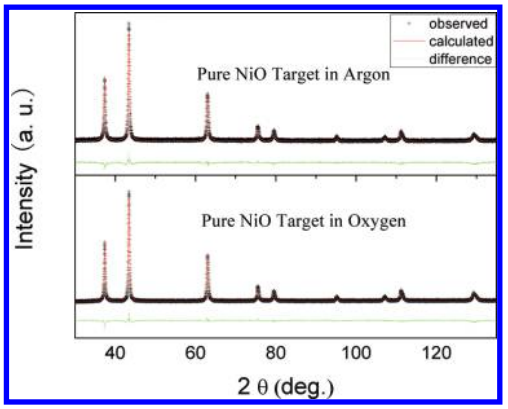

Figure 2. Rietveld refinement patterns for the NiO nanocrystals evaporated from the pure NiO target. The observed diffraction intensities and the calculated patterns are represented by the plus signs and the solid lines, respectively. The dashed line at the bottom of each pattern represents the difference.

of samples evaporated directly from the NiO. All the diffraction peaks can be indexed to cubic structure NiO. The structure refinement was performed using a Rietveld analysis program (Rietica V1.7.7). We adopted the space group *Fm*3*m*, and the final fitting factors were quite low, decreasing to R_p = 7.38%, R_{wp} = 8.96%, and R_{exp} = 3.70% for the sample grown in 100 cc/min argon flow, and R_p = 6.43%, R_{wp} = 7.78%, and R_{exp} = 3.87% for the sample grown in 100 cc/min oxygen flow. The lattice parameters are a = 4.1783(3) Å and a = 4.1779(1) Å, respectively. The lattice parameter values agree well with standard cubic structure NiO (PDF 47-1049). The particle size and the strain were calculated from Williamsom–Hall plots by using the full width at half-maximum (fwhm) of the diffraction peaks.[30] We estimate the average particle size and strain to be 28.7(3) nm and 0.052(3)% for the nanocrystals grown in argon flow and 34.9(2) nm and 0.043(1)% for the nanocrystals grown in oxygen flow.

Figure 3 shows FE-SEM and TEM images of the NiO nanocrystals directly evaporated from the pure NiO target. It was found that the NiO nanocrystals grown in flowing oxygen were cubic particles (Figure 3a,b) 10–70 nm in width. When the growth was performed in flowing argon with other conditions kept constant, the nanocrystals were mixtures of cubic shaped particles and nanorods (see Figure 3c), in which particles were cubic shaped and 10–45 nm in width, while the nanorods had an average width of 15 nm and an aspect ratio of 3–10, indicating that the growth atmosphere strongly influences the morphology under these growth conditions. These nanocrystals have smooth surfaces, and the atomic fringe spacing corresponds to the interplanar distance between the (200) planes.

The nanocrystals were grown by this physical vapor deposition method without the introduction of any metal

dx.doi.org/10.1021/cg201676u | *Cryst. Growth Des.* 2012, 12, 2842–2849

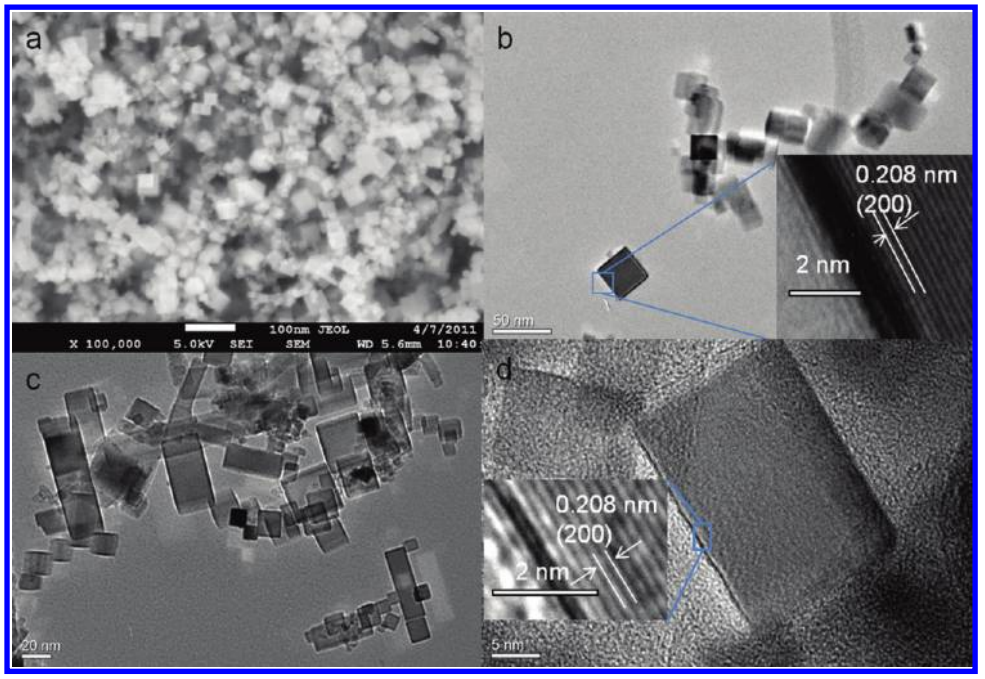

Figure 3. FE-SEM (a) and TEM (b–d) images of nanocrystals evaporated from the pure NiO target: (a, b) samples grown in 100 cc/min flowing oxygen, (c, d) samples grown in 100 cc/min flowing argon. The insets in panels b and d are at higher magnification and show the lattice spacing.

catalyst. Vapor–solid (VS) and vapor–liquid–solid (VLS) mechanisms have been widely used to explain the formation of one-dimensional nanocrystals.[31−34] According to the VLS growth mechanism, a liquid droplet (metal catalyst) will guide the crystal growth. Our FE-SEM and TEM images, however, as in Figure 3, did not show any globules at the tips of the nanorods, nor do any spherical impurities appear in either the nanoparticles or the nanorods. We propose that the growth was governed by the VS process. The process involved in the growth from the pure target could be described as follows:

$$2NiO(s) \rightarrow 2Ni(g) + O_2(g) \quad (1)$$

$$2Ni(g) + O_2 \rightarrow 2NiO(s) \quad (2)$$

During the reactions, the solid NiO decomposes at high temperature, and the Ni and O_2 gases that are produced flow to the low-temperature region and react with each other to form NiO again. When the supersaturation is increased near the heating area, stoichiometric nuclei form in order to balance the local charge and achieve structural symmetry. Newly arriving vapor will be deposited on the formed nuclei, while the surfaces that have lower energy start to form. Because the temperature in this region is high, the low-energy surfaces tend to be flat. As the distance from the target increases, the vapor concentration and temperature decrease rapidly, and the crystallization process will stop when the supersaturation and temperature have been reduced to a critical point. The fully formed nanocrystals are then deposited on the quartz tube (T < 400 °C). Oxide nanostructures formed in the low-temperature region were always found to have oxygen vacancy point defects, stacking faults, and twinning.[32] In our TEM results, no defects are detectable throughout the nanocrystals, indicating that the nanocrystals are formed in a relatively high-temperature region and the samples are more likely to be stoichiometric NiO rather than Ni-deficient NiO.

Samples collected from the filter of the gas outlet and different positions on the quartz tube were characterized by FE-SEM and TEM; the results show that the nanocrystals have similar shapes and size distributions. As the growth time was increased from 6 to 12 h under flowing argon, the amount of the product increased from 45 to 76 mg, but the morphologies, diameters, and lengths of the nanocrystals were not significantly different. So, we consider that crystal growth mainly occurred in the carrier gas rather than on the quartz tube. When growth took place in argon atmosphere, the vapor concentration and the partial pressure of oxygen were lower than when growth took place in oxygen atmosphere, thus yielding low vapor supersaturation, and this could be the main reason for the formation of nanorods and the lower yield under these conditions.

Nanocrystal growth based on the bottom-up approach has advantages when creating structures with dimensions below 10 nm. Our efforts, however, to decrease the crystal size below 10 nm by using pure NiO target were not successful. It has been revealed that the growth temperature and the supersaturation ratio are the two dominant processing factors for controlling the size and morphology of the nanocrystals in the VS growth process.[32] In order to fabricate monodisperse NiO nanoparticles with sizes smaller than 10 nm, we propose that reducing the supersaturation of the vapor phase while maintaining the high temperature of the heating area will be helpful in this method. TiO_2 has a high melting point (1800 °C) and very low vapor pressure at high temperature, and the $NiTiO_3$ that is initially produced in the target along with excess NiO also has a high melting point (1690 °C) and is stable at high temperature. Therefore, a NiO–TiO_2 mixed target was chosen, because it was possible to evaporate the NiO below the melting point of $NiTiO_3$ and greatly reduce the supersaturation of the vapor from a small amount of excess NiO.

In the initial experiments, 100 cm^3/min flowing oxygen was used as the carrier gas. It was found that after 6 h of growth at 1680 °C, only a tiny amount (less than 1 mg) of nanomaterials could be collected from the inner wall of the quartz tube. The amount of product was not enough for further characterization

and property measurements. When the high purity argon gas was used, the volatility of NiO increased, and a layer of gray-green nanocrystals formed after 2 h of heating, indicating that the atmosphere significantly influences the volatility of NiO in this system. The nanocrystal growth from the mixed target was performed at approximately 1680 °C. The products were formed on the inner wall of the quartz tube located downstream of the carrier gases at a distance of 25−180 mm from the middle of the heating area, where the growth temperature was estimated to be in the range of 150−400 °C. After 24 h of growth, more than 19 and 25 mg of product were obtained with flow rates of 100 and 500 cc/min, respectively. As-grown nanocrystals were collected from the quartz tube for the following characterizations.

The XRD patterns obtained from the two samples clearly indicate that there are no traces of impurities in our samples. All of the peaks of each pattern can be indexed to the cubic structure. The EDX patterns (Figure S1, Supporting Information) of the nanocrystals show only peaks of C, O, and Ni, where the C peak originates from the conductive carbon tape, further confirming the formation of pure NiO without any detectable impurities in our samples. The structure refinement was performed using a Rietveld analysis program (Rietica V1.7.7). We adopted the space group *Fm*3*m*, and Figure 4 presents the refinement patterns of the samples. The

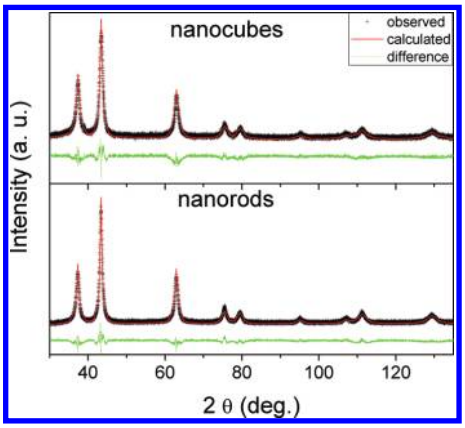

Figure 4. Rietveld refinement patterns for the NiO nanocrystals grown from the mixed target. The observed diffraction intensities and the calculated patterns are represented by the plus signs and the solid lines, respectively. The dashed line at the bottom of each pattern represents the difference.

final fitting factors were quite low, decreasing to R_p = 7.11%, R_{wp} = 8.87%, and R_{exp} = 5.29% for the sample grown in 100 cc/min argon flow, and R_p = 6.80%, R_{wp} = 8.32%, and R_{exp} = 4.53% for the sample grown in 500 cc/min argon flow. The cell parameters are a = 4.187(4) Å and a = 4.1907(6) Å, respectively. The cell parameter values agree with standard cubic structure NiO (PDF 47-1049) and only show tiny lattice expansion.

From the Williamson−Hall plots, we estimate the average particle size and strain to be 8.1(2) nm and 0.045(24)% for the nanocrystals grown in 100 cc/min argon flow and 12.2(2) nm and 0.12(1)% for the nanocrystals grown in 500 cc/min argon flow. TEM images (Figures 5 and 6) further confirm that they are nanocubes and nanorods, respectively. The strain value of the nanorod sample is 2.7 times that of the nanocube sample, and this ratio is close to the average surface area ratio for these two samples, so we mainly attribute the strain to the broken symmetry at the surface and broken bonds. The quality of the samples is revealed by the TEM images, where most of the nanocrystals show smooth surfaces and clear-cut edges, indicating that the nanocrystals grown by our method can be used as a model system for size effect research.

Figure 5 presents TEM images of nanocrystals grown in 100 cc/min argon flow rate. It is found that most of the nanocrystals have a cubic shape with an average size of 8 nm, while only a very few particles are tetragonal in shape with an aspect ratio of less than 2. The SAED pattern is shown in the inset of Figure 5b and can be indexed as a cubic structure. The ratio $R_1^2/R_2^2/R_3^2$ = 3:4:8, which agrees well with the fcc structure. The high-resolution TEM (HRTEM) images show a lattice spacing of 2.08 Å for the particles in Figure 5d. These particles have smooth surfaces down to the atomic scale and straight edges parallel to (100) equivalent crystal planes. All the atoms are arranged in perfect lines throughout the entire particle, indicating the highly crystalline nature of these nanocubes. We propose a layer-by-layer growth mode, since step-like defects, one to several atomic layers in width, appear on the edges, as shown in the inset of Figure 5d.

The TEM images in Figure 6 show the sample grown with the 500 cc/min argon flow rate. Figure 6a,b indicates that most of the nanocrystals are tetragonal rods with an average width of 6 nm and an aspect ratio of 2−6, with only a tiny amount of nanocubes present. The SAED pattern (inset of Figure 5b) indicates that the NiO specimen is crystallized in the fcc structure. The HRTEM images shown in Figure 6b−h clearly demonstrate the highly crystalline nature of the NiO nanorods. All of the atomic fringe spacing corresponds to the interplanar distance between the (200) planes, and the nanorods have grown along the (100) equivalent directions.

Based on the TEM results, we propose that the growth model for our experiments is a VS growth mechanism. The chemical reactions involved in the growth could be described as follows:

$$(1+\delta)\mathrm{NiO(s)} + \mathrm{TiO_2(s)} \rightarrow \mathrm{NiTiO_3(s)} + \delta\mathrm{Ni(g)} + \delta/2\mathrm{O_2(g)} \quad (3)$$

$$\delta\mathrm{Ni(g)} + \delta/2\mathrm{O_2} \rightarrow \delta\mathrm{NiO(s)} \quad (4)$$

During the reactions, the solid NiO reacts with TiO_2 to produce $NiTiO_3$, and the extra NiO decomposes at high temperature. The XRD pattern obtained from the mixed target after the growth indicates only the presence of $NiTiO_3$ (Figure S2, Supporting Information). The Ni and O_2 gases that are produced flow to the lower temperature region and react with each other to form solid NiO again. Because the vapor concentration from the mixed target is lower than that from the pure target, the amount of products is also lower. When growth is performed in oxygen atmosphere, the amount of vapor generated by reaction 3 is reduced because of the higher partial pressure of oxygen. Therefore, only a tiny amount of product was obtained under this condition. When growth was performed under flowing argon, the nanocrystal growth occurred in a precipitation process. Stoichiometric nuclei are formed near the heating area, and newly arriving vapor will be deposited on the formed nuclei, while the surfaces that have lower energy start to form, such as the side surfaces. Because the temperature in this region is high, the low-energy surfaces tend to be flat, and more incoming vapor will accumulate on

dx.doi.org/10.1021/cg201676u | *Cryst. Growth Des.* 2012, 12, 2842−2849

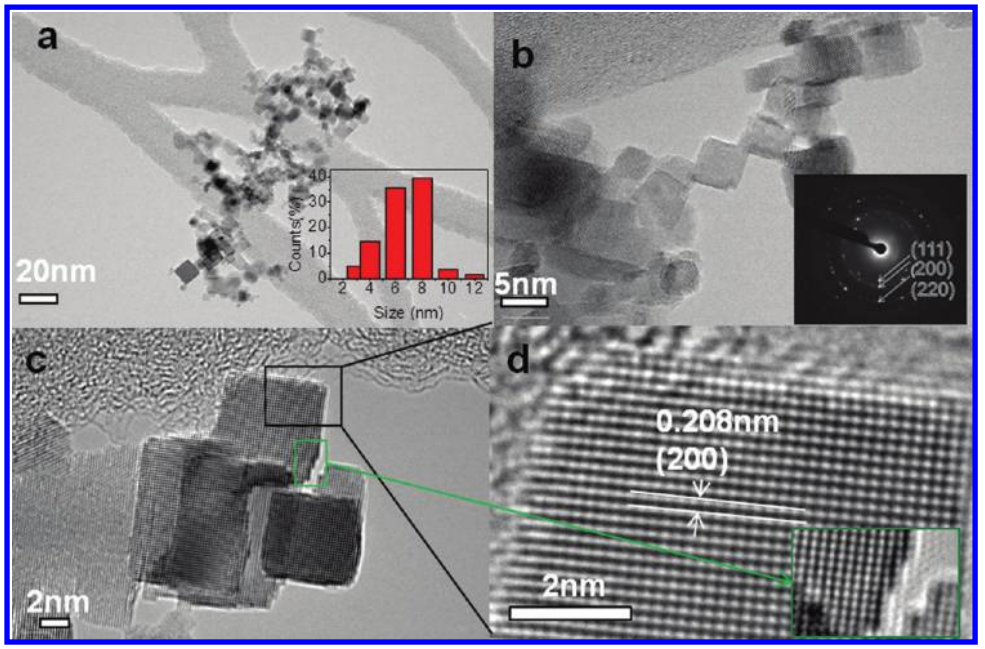

Figure 5. TEM images of NiO nanocubes with regular cubic shape that were evaporated from the mixed target in 100 cc/min argon flow rate: (a) Low-resolution TEM image with the inset showing the histogram of the particle size distribution. The long rods present in the background of panel a are the TEM grid. (b, c) High-resolution images, the inset of (b) showing the corresponding SAED pattern. (d) The magnified images of the square areas marked in panel c, with the inset showing the step-like defects at the edges of the nanocrystals.

the relatively rough growth front (Figures 5d and 6c), leading to the fast formation of a nanocube or nanorod. A higher flow rate will speed up reaction 3 and quickly carry the vapor to a relatively low temperature region, thus producing more nanocrystals than a lower flow rate. Meanwhile, the concentration of the vapor is reduced, thus yielding low vapor supersaturation. This could be the main reason for the formation of nanorods in 500 cc/min flowing argon.

Our experiments show that the products are highly crystalline nanomaterials with regular surfaces, and the (100) equivalent crystal planes are exposed on the surfaces. No defects are evident in any of the HRTEM images. This finding is in agreement with the findings for bulk surfaces and nanoparticles. It was reported that the (100) surfaces were the most readily oxidized at high temperature.[35,36] The reason nanocrystal growth governed by the VS process usually yields nanostructures with faceted shapes that consist of certain low index crystallographic planes is not clear in the present study. However, this method has some unique features compared with other existing physical approaches for growing nanocrystals of oxides or non-oxides.[32,34] Infrared heating evaporation involves processing in an optical floating zone furnace, where the heating area can be controlled down to a very small range, usually smaller than 3 mm, which is almost the width of the filament of the supplied lamp (300 W); this can give rise to a very sharp temperature gradient along the vertical direction (more than 300 °C/cm). When the gas flows through the heating area, the hot vapor species are quickly carried to the low temperature area, condense into small nuclei, and start to grow along their easy growth directions. The growth of the nanocrystals will be stopped when the vapor supersaturation or temperature are reduced to a critical point.

Based on the unique features of this method, we predict that infrared heating evaporation from a mixed target can be extended to many other materials, especially for compounds that are not directly suitable for the other evaporation methods, opening up new opportunities in nanomaterials science and technology.

We will use the average particle size obtained from X-ray diffraction in the following discussion. Figure 7 shows the magnetic hysteresis loops measured in the zero-field-cooled (ZFC) condition at 5 and 305 K. It reveals that hysteresis is clearly present at 5 K for the nanocrystals grown from the mixed target (8 and 12 nm) but only shows a linear dependence of the magnetization on the applied field for the samples grown from the pure NiO target (29 and 35 nm). However, a small amount of hysteresis is also observed at 5 K in these two samples, as shown in the inset of Figure 7a, indicating uncompensated spins at the surface of these nanocrystals. A weak ferromagnetic state persists at 305 K for the samples with sizes smaller than 12 nm. However, the hysteresis is barely visible for either sample, indicating extremely small coercive fields. The nanocrystals grown from the pure NiO target with average particle sizes larger than 29 nm only show a linear dependence of magnetization at 305 K. This behavior has been previously reported in nanoparticles,[37] and the results indicate that the high-temperature magnetic behavior of the larger size nanocrystals is dominated by an uncompensated antiferromagnetic core moment contribution.

The temperature dependence of the susceptibility for the nanocrystal samples measured under ZFC and field-cooled (FC) conditions in a field of 1000 Oe is shown in Figure 8. Upon cooling, a discrepancy between the ZFC and FC curves appears below the bifurcation temperature, T_{irr} = 230 K, and a broad peak at the blocking temperature, T_b = 183 K, in the ZFC curve is found for the 12 nm nanorods. This sample also shows the largest magnetization in the high-temperature range. This can be attributed to the greater degree of broken symmetry at the surface and the higher proportion of broken bonds.[38] All of the other samples show similar features over a wide temperature range, and their magnetization decreases with particle size. This behavior supports the intuitive picture that

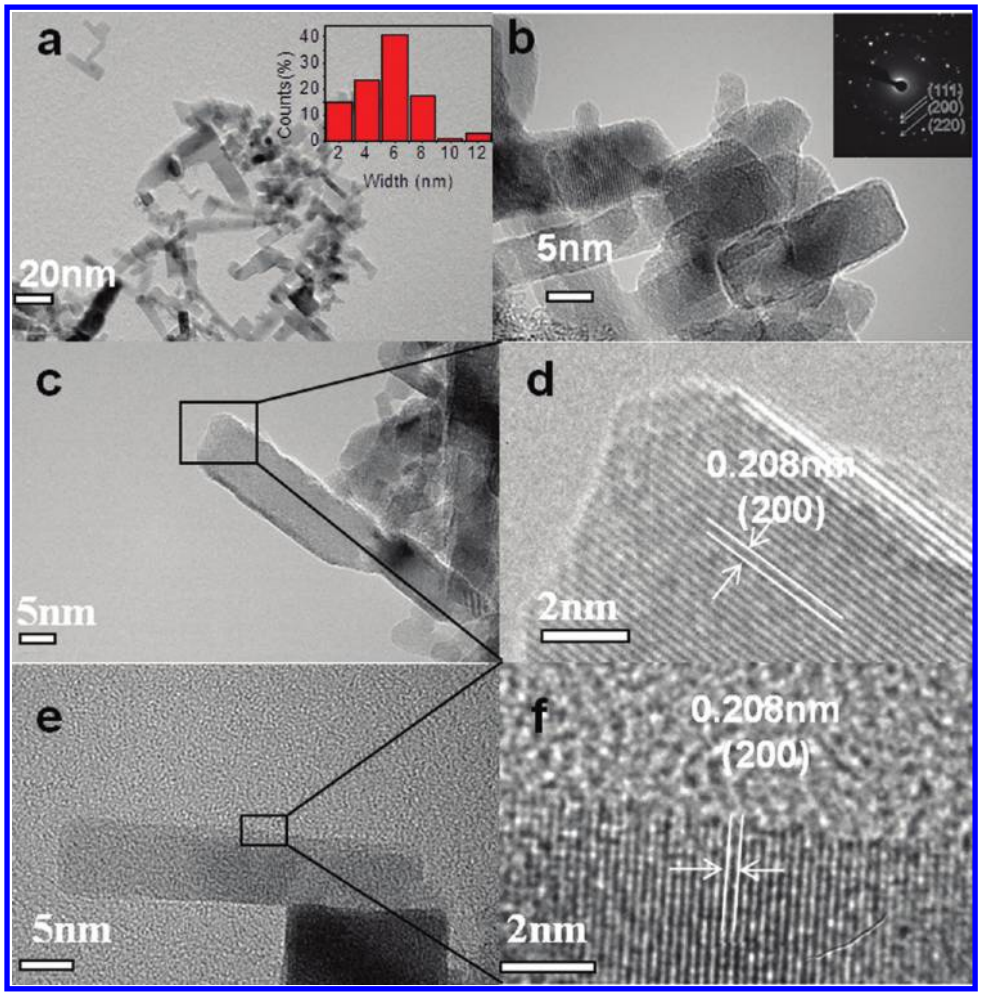

Figure 6. TEM images of NiO nanorods that were grown from the mixed target in 500 cc/min argon flow rate: (a) Low-resolution TEM image with the inset showing the histogram of the width distribution of the nanorods. (b, c, e) High-resolution images with the inset of panel b showing the corresponding SAED pattern. (d, f) Magnified images of the square areas marked in panels c and e, respectively.

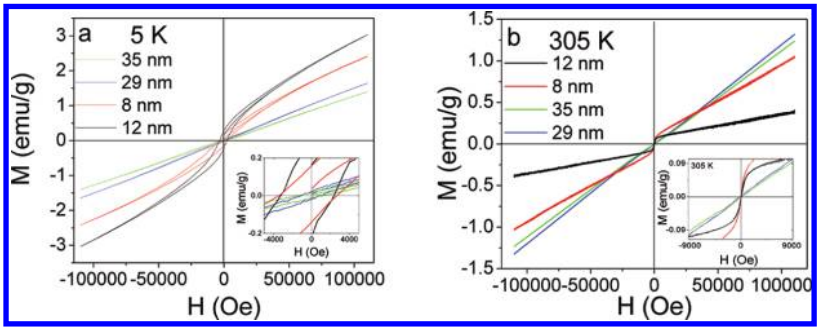

Figure 7. Magnetization hysteresis loops at 5 K (a) and 305 K (b) for NiO nanocrystals of different sizes. The insets are the loops on an expanded scale around $H = 0$.

smaller particles should yield a larger fraction of uncompensated surface spins and hence larger magnetization.[21] As shown in inset of Figure 8b, the bifurcation temperature, T_{irr}, seems to increase with decreasing particle size. The blocking temperature T_b, however, does not show any trend with the average particle size for our samples. Earlier research has revealed that the blocking temperature decreases with the particle size,[38,39] but such behavior was found in nanoparticles with similar shape, while the samples in the present study are nanocubes (8 and 35 nm), a nanocube and nanorod mixture (29 nm), and nanorods (12 nm). Since the magnetic properties in this study cannot be easily attributed to the average size, the lattice expansion, or the strain values, we suggest that the particle size, lattice perfection, surface orientation, and smoothness of the particle surface may play key roles in determining the magnetic states in the nanocrystals studied in this work. Further investigations on the mechanism behind the surface and bulk states in NiO nanocrystals are underway in our laboratory.

■ CONCLUSION

Nickel oxide nanocrystals can be directly evaporated from pure NiO target by using the infrared heating evaporation method;

dx.doi.org/10.1021/cg201676u | *Cryst. Growth Des.* 2012, 12, 2842–2849

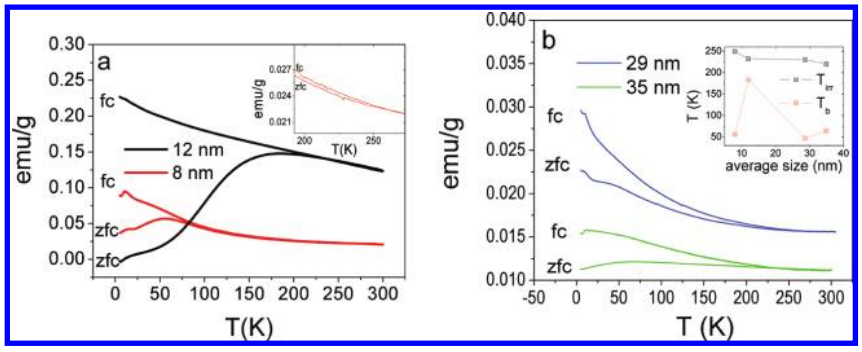

Figure 8. Temperature dependence of the susceptibility measured in 1000 Oe magnetic field for nanocrystals of different sizes grown from the mixed target (a) and the pure NiO target (b). The inset of panel a is an expanded scale around T = 230 K for the 8 nm nanocubes. The inset in panel b shows T_{irr} and T_b vs particle size.

these nanocrystals have a wide size distribution and are larger in size, from 10 to 150 nm. The growth atmosphere strongly influences the morphology and size. Nanocubes and nanorods with small average sizes of 8 and 12 nm have been synthesized from the mixed target. The morphology of the nanomaterials can be tuned by the gas flow rate. No impurity phases were detected by XRD, EDX, or SAED. Both the nanocubes and the tetragonal nanorods are highly crystallized. The formation of nanorods is achieved by a higher gas flow rate in the reaction chamber. A layer-by-layer growth mode and a vapor−solid mechanism growth model are proposed. This new approach for highly crystallized nanomaterials can be applied to other materials and will trigger more study in both methodology and nanomaterials science.

■ ASSOCIATED CONTENT

Supporting Information

The EDX patterns of products, XRD pattern of the mixed target after growth, and detailed refinement information of NiO nanocrystals grown from mixed target. This information is available free of charge via the Internet at http://pubs.acs.org/.

■ AUTHOR INFORMATION

Corresponding Author

*E-mail: xiaolin@uow.edu.au.

Notes

The authors declare no competing financial interest.

■ ACKNOWLEDGMENTS

This work is supported by funding from the Australian Research Council through Discovery Projects DP0987190 and DP0558753. D. P. Chen is supported by an ARC APD fellowship. We thank Dr. Tania Silver at the University of Wollongong for critical reading of the manuscript.

■ REFERENCES

(1) Rao, C. N. R. *Annu. Rev. Phys. Chem.* **1989**, *40*, 291−326.
(2) Tokura, Y.; Nagaosa, N. *Science* **2000**, *288*, 462−468.
(3) Lee, M.-J.; Han, S.; Jeon, S. H.; Park, B. H.; Kang, B. S.; Ahn, S.-E.; Kim, K. H.; Lee, C. B.; Kim, C. J.; Yoo, I.-K.; Seo, D. H.; Li, X.-S.; Park, J.-B.; Lee, J.-H.; Park, Y. *Nano Lett.* **2009**, *9*, 1476−1481.
(4) Gibbons, J. F.; Beadle, W. E. *Solid-State Electron.* **1964**, *7*, 785−797.
(5) Lee, H.-D.; Magyari-Köpe, B.; Nishi, Y. *Phys. Rev. B* **2010**, *81*, 193202.
(6) Oka, K.; Yanagida, T.; Nagashima, K.; Kawai, T.; Kim, J.-S.; Park, B.-H. *J. Am. Chem. Soc.* **2010**, *132*, 6634−6635.
(7) Duong, N. P.; Satoh, T.; Fiebig, M. *Phys. Rev. Lett.* **2004**, *93*, No. 117402.
(8) Satoh, T.; Cho, S.-J.; Iida, R.; Shimura, T.; Kuroda, K.; Ueda, H.; Ueda, Y.; Ivanov, B. A.; Nori, F.; Fiebig, M. *Phys. Rev. Lett.* **2010**, *105*, No. 077402.
(9) Roth, W. L. *Phys. Rev.* **1958**, *110*, 1333−1341.
(10) Stohr, J.; Scholl, A.; Regan, T. J.; Anders, S.; Luning, J.; Scheinfein, M. R.; Padmore, H. A.; White, R. L. *Phys. Rev. Lett.* **1999**, *83*, 1862−1865.
(11) Hutchings, M. T.; Samuelsen, E. J. *Phys. Rev. B* **1972**, *6*, 3447−3461.
(12) Milano, J.; Grimsditch, M. *Phys. Rev. B* **2010**, *81*, No. 094415.
(13) Poizot, P.; Laruelle, S.; Grugeon, S.; Dupont, L.; Tarascon, J.-M. *Nature* **2000**, *407*, 496−499.
(14) Li, X.; Dhanabalan, A.; Bechtold, K.; Wang, C. *Electrochem. Commun.* **2010**, *12*, 1222−1225.
(15) Zhang, X.; Shi, W.; Zhu, J.; Zhao, W.; Ma, J.; Mhaisalkar, S.; Maria, T.-L.; Yang, Y.; Zhang, H.; Hng, H.-H.; Yan, Q. *Nano Res.* **2010**, *3*, 643−652.
(16) Tao, B.; Zhang, J.; Miao, F.; Hui, S.; Wan, L. *Electrochim. Acta* **2010**, *55*, 5258−5262.
(17) Wang, Y.; Zhu, J.; Yang, X.; Lu, L.; Wang, X. *Thermochim. Acta* **2005**, *437*, 106−109.
(18) Aslani, A.; Oroojpour, V.; Fallahi, M. *Appl. Surf. Sci.* **2011**, *257*, 4056−4061.
(19) Kim, J.; Piao, Y.; Lee, N.; Park, Y.; Lee, I.-H.; Lee, J.-H.; Paik, S. R.; Hyeon, T. *Adv. Mater.* **2010**, *22*, 57−60.
(20) Mandal, S.; Banerjee, S.; Menon, K. S. R. *Phys. Rev. B* **2009**, *80*, No. 214420.
(21) Kodama, R. H.; Makhlouf, S. A.; Ferkowitz, A. E. *Phys. Rev. Lett.* **1997**, *79*, 1393−1396.
(22) Wang, X.; Yu, L.; Hu, P.; Yuan, F. *Cryst. Growth Des.* **2007**, *7*, 2415−2418.
(23) Wang, W.; Liu, Y.; Xu, C.; Zheng, C.; Wang, G. *Chem. Phys. Lett.* **2002**, *362*, 119−122.
(24) Lenggoro, I. W.; Itoh, Y.; Iida, N.; Okuyama, K. *Mater. Res. Bull.* **2003**, *38*, 1819−1827.
(25) Yang, Q.; Sha, J.; Ma, X.; Yang, D. *Mater. Lett.* **2005**, *59*, 1967−1970.
(26) Ghosh, M.; Biswas, K.; Sundaresan, A.; Rao, C. N. R. *J. Mater. Chem.* **2006**, *16*, 106−111.
(27) Hu, J.; Zhu, K.; Chen, L.; Yang, H.; Li, Z.; Suchopar, A.; Richards, R. *Adv. Mater.* **2008**, *20*, 267−271.
(28) Ge, M. Y.; Han, L. Y.; Wiedwald, U.; Xu, X. B.; Wang, C.; Kuepper, K.; Ziemann, P.; Jiang, J. Z. *Nanotechnology* **2010**, *21*, 425702.
(29) Porqueras, I.; Bertran, E. *Thin Solid Films* **2001**, *398*−*399*, 41−44.
(30) Qadri, S. B.; Skelton, E. F.; Hsu, D.; Dinsmore, A. D.; Yang, J.; Gray, H. F.; Ratna, B. R. *Phys. Rev. B* **1999**, *60*, 9191−9193.
(31) Brenner, S. S.; Sears, G. W. *Acta Metall.* **1956**, *4*, 268−270.

(32) Dai, Z. R.; Pan, Z. W.; Wang, Z. L. *Adv. Funct. Mater.* **2003**, *13*, 9−24.
(33) Wagner, R. S.; Ellis, W. C. *Appl. Phys. Lett.* **1964**, *4*, 89−90.
(34) Duan, X. F.; Lieber, C. M. *Adv. Mater.* **2000**, *12*, 298.
(35) Feygenson, M.; Kou, A.; Kreno, L. E.; Tiano, A. L.; Patete, J. M.; Zheng, F.; Kim, M. S.; Solovyov, V.; Wong, S. S.; Aronson, M. C. *Phys. Rev. B* **2010**, *81*, No. 014420.
(36) Woodcock, S. A.; Abell, J. S.; Eickemeyer, J.; Holzapfel, B. *J. Microsc.* **2004**, *216*, 123−130.
(37) Winkler, E.; Zysler, R. D.; Mansilla, M. V.; Fiorani, D. *Phys. Rev. B* **2005**, *72*, 132409.
(38) Makhlouf, S. A.; Parker, F. T.; Spada, F. E.; Berkowitz, A. E. *J. Appl. Phys.* **1997**, *81*, 5561−5563.
(39) Shim, H.; Dutta, P.; Seehra, M. S.; Bonevich, J. *Solid State Commun.* **2008**, *145*, 192−196.